



1    **Abstract**

2       Spin-echo (SE) BOLD fMRI has high microvascular specificity, and thus provides a more reliable  
3    means to localize neural activity compared to conventional gradient-echo BOLD fMRI. However, the most  
4    common SE BOLD acquisition method, SE-EPI, is known to suffer from  $T_2'$  contrast contamination with  
5    undesirable draining vein bias. To address this, in this study, we extended a recently developed  
6    distortion/blurring-free multi-shot EPI technique, Echo-Planar Time-resolved Imaging (EPTI), to cortical-  
7    depth dependent SE-fMRI at 7T to test whether it could provide purer SE BOLD contrast with minimal  $T_2'$   
8    contamination for improved neuronal specificity. From the same acquisition, the time-resolved feature of  
9    EPTI also provides a series of asymmetric SE (ASE) images with varying  $T_2'$  weightings, and enables  
10   extraction of data equivalent to conventional SE EPI with different echo train lengths (ETLs). This allows  
11   us to systematically examine how  $T_2'$ -contribution affects different SE acquisition strategies using a single  
12   dataset. A low-rank spatiotemporal subspace reconstruction was implemented for the SE-EPTI acquisition,  
13   which incorporates corrections for both shot-to-shot phase variations and dynamic  $B_0$  drifts. SE-EPTI was  
14   used in a visual task fMRI experiment to demonstrate that i) the pure SE image provided by EPTI results  
15   in the highest microvascular specificity; ii) the ASE EPTI series, with a graded introduction of  $T_2'$   
16   weightings at time points farther away from the pure SE, show a gradual sensitivity increase along with  
17   increasing draining vein bias; iii) the longer ETL seen in conventional SE EPI acquisitions will induce more  
18   draining vein bias. Consistent results were observed across multiple subjects, demonstrating the robustness  
19   of the proposed technique for SE-BOLD fMRI with high specificity.

20

21

22

23    **Key Words:** high field, multi-echo, spin-echo,  $T_2$  BOLD, microvascular specificity, laminar fMRI

24

## 1 1. Introduction

2 Gradient-echo (GE) blood oxygenation level-dependent (BOLD) with  $T_2^*$  weighting is one of the most  
3 commonly used fMRI contrasts due to its high sensitivity and acquisition efficiency (Bandettini et al., 1992;  
4 Kwong et al., 1992; Ogawa et al., 1990). However, the GE BOLD signal contains a mixture of contributions  
5 from both large and small blood vessels. The macrovascular signals, such as those from large draining veins,  
6 can be far from the site of neuronal activity (Havlicek and Uludağ, 2020; Heinze et al., 2016; Markuerkiaga  
7 et al., 2016). Therefore, the inclusion of macrovascular signal in GE BOLD fMRI significantly limits its  
8 effective resolution to detect brain activity, even at high spatial resolution at ultra-high-field.

9 Conversely, the microvascular signal can provide more specific and precise localization of the  
10 neuronal activity (Dumoulin et al., 2018; Norris and Polimeni, 2019), therefore, a number of alternative  
11 fMRI contrasts have been investigated that have the promise of achieving high neuronal specificity through  
12 being sensitive to signal changes from the microvasculature while being insensitive to changes from the  
13 macrovasculature (De Martino et al., 2018; Huber et al., 2019; Koopmans and Yacoub, 2019). Among those,  
14 spin-echo (SE) or  $T_2$  BOLD fMRI has shown great potential (Bandettini and Wong, 1995; Boxerman et al.,  
15 1995; Ogawa et al., 1993) and has been demonstrated to provide superior specificity compared to GE BOLD  
16 (Huber et al., 2017a). However, it is difficult to efficiently obtain pure  $T_2$ -weighting without  $T_2'$   
17 contamination (Norris, 2012), which introduces unwanted sensitivity to the microvasculature and thus  
18 compromises its achievable neuronal specificity.

19 This difficulty originates from the technical challenges in conventional MRI acquisition. For example,  
20 the most commonly-used  $T_2$  BOLD acquisition method, spin-echo EPI, uses a long echo-train-length (ETL)  
21 that samples both  $T_2$ - and  $T_2'$ -weighted signals to generate an image, and therefore suffers from  $T_2'$   
22 contamination with an undesirable sensitivity to large blood vessels (Bandettini et al., 1994; Birn and  
23 Bandettini, 2002; Duyn, 2004; Goense and Logothetis, 2006; Koopmans and Yacoub, 2019; Norris, 2012;  
24 Yacoub et al., 2003). In-plane acceleration with parallel imaging (Griswold et al., 2002; Pruessmann et al.,  
25 1999a; Sodickson and Manning, 1997) or multi-shot EPI (ms-EPI) (Butts et al., 1996; Chen et al., 2013;  
26 Dong et al., 2018; Jeong et al., 2013; Mani et al., 2017) can be used to address this issue by reducing the  
27 effective echo spacing and thus the ETL. However, their abilities to reduce  $T_2'$  contribution come at a cost  
28 of higher noise amplification or image artifacts due to shot-to-shot phase variations, and residual  $T_2'$   
29 contamination as well as distortion and blurring still remains. Other alternative sequences have been  
30 proposed to provide  $T_2$  BOLD contrast (Barth et al., 2010; Bowen et al., 2005; Chamberlain et al., 2007;  
31 Constable et al., 1994; Denolin and Metens, 2003; Goerke et al., 2011; Miller et al., 2003; Polimeni et al.,  
32 2017; Poser and Norris, 2007; Scheffler et al., 2001). Among those, 3D-GRASE uses multiple refocusing  
33 pulses with short echo trains in between, which significantly reduces the  $T_2'$  weightings and offers higher  
34 specificity than conventional SE-EPI (Beckett et al., 2020; De Martino et al., 2013; Feinberg et al., 2008;

1 Kemper et al., 2015; Olman et al., 2012; Park et al., 2021). Recent works have demonstrated its specificity  
2 for high-resolution SE BOLD fMRI at 7T (Beckett et al., 2020; Kemper et al., 2015), but challenges  
3 including high SAR, relatively small achievable coverage and a mixture of  $T_1$  weightings from stimulated  
4 echoes (Goerke et al., 2007) remain to be addressed or interpreted. In addition to SE BOLD fMRI, non-  
5 BOLD contrasts such as cerebral blood volume (CBV) has shown promising results as well, such as using  
6 the vascular space occupancy (VASO) methods (Chai et al., 2020; Huber et al., 2020; Huber et al., 2014;  
7 Huber et al., 2019; Jin and Kim, 2006; Lu et al., 2003; Lu et al., 2004).

8 In this study, to address the  $T_2'$ -contamination of SE-EPI and obtain higher neuronal specificity with  
9 reduced draining vein effects, we extended a recently developed technique, Echo-Planar Time-resolved  
10 Imaging (EPTI) (Wang et al., 2019; Wang et al., 2020; Wang et al., 2021b), to high-resolution SE-fMRI at  
11 ultra-high-field for mapping laminar fMRI responses. EPTI is a novel multi-shot EPI approach that has  
12 been previously developed for efficient multi-contrast and quantitative mapping. It employs a novel  
13 spatiotemporal encoding strategy in the frequency-echo ( $k$ - $t$ ) domain, and is therefore able to resolve a  
14 series of multi-contrast images across the readout with a small TE increment as short as an echo spacing  
15 (~1 ms). The images are also distortion- and blurring-free, providing accurate anatomical information for  
16 high-resolution imaging. In addition, the continuous signal readout scheme and the use of spatiotemporal  
17 correlation to recover the  $k$ - $t$  undersampled data in EPTI result in high acquisition efficiency, allowing us  
18 to acquire multi-echo images at submillimeter isotropic resolution within a few shots.

19 Here, we show that the time-resolved feature of EPTI can not only provide pure  $T_2$  contrast images to  
20 increase microvascular specificity, but can also simultaneously acquire  $T_2'$ -weighted images to investigate  
21 the macrovascular contribution across the spin-echo readout. Specifically, using a SE-EPTI acquisition, we  
22 obtained a pure SE image with minimal  $T_2'$  contamination, and a series of asymmetric SE (ASE) images  
23 with varying  $T_2'$  weightings. We also developed a framework to extract conventional SE ms-EPI images  
24 with different ETLs (therefore with different levels of  $T_2'$ -contamination) from the same dataset, but without  
25 any distortion. This ensures that all images concurrently acquired in a SE-EPTI acquisition, including the  
26 pure SE, ASEs and the extracted conventional SE-EPIs are perfectly matched and aligned. A subspace  
27 reconstruction (Dong et al., 2020; Guo et al., 2021; He et al., 2016; Lam and Liang, 2014; Liang, 2007;  
28 Meng et al., 2021; Tamir et al., 2017) was further implemented for SE-EPTI datasets, which incorporates  
29 corrections for both dynamic  $B_0$  drifts and shot-to-shot phase variations caused by respiration or other  
30 physiological factors. A 3-shot SE-EPTI protocol was developed to acquire a thick slab that sufficiently  
31 covers the visual cortex at submillimeter resolution (0.9 mm isotropic). Through cortical depth analyses,  
32 we demonstrated that the pure SE BOLD data provided by EPTI results in the highest microvascular  
33 specificity as expected, and the ASE EPTI image series, with a graded introduction of  $T_2'$  weightings at  
34 time points farther away from the pure SE, show gradually increased sensitivity, but larger and larger

1 draining vein bias. Using the same dataset, we also experimentally confirmed that a longer ETL in the  
2 conventional SE EPI acquisition will induce more draining vessel bias. We present consistent results across  
3 multiple subjects, demonstrating the robustness of the proposed technique and framework.

4 **2. Material and methods**

5 *2.1. EPTI for pure contrast multi-echo imaging*

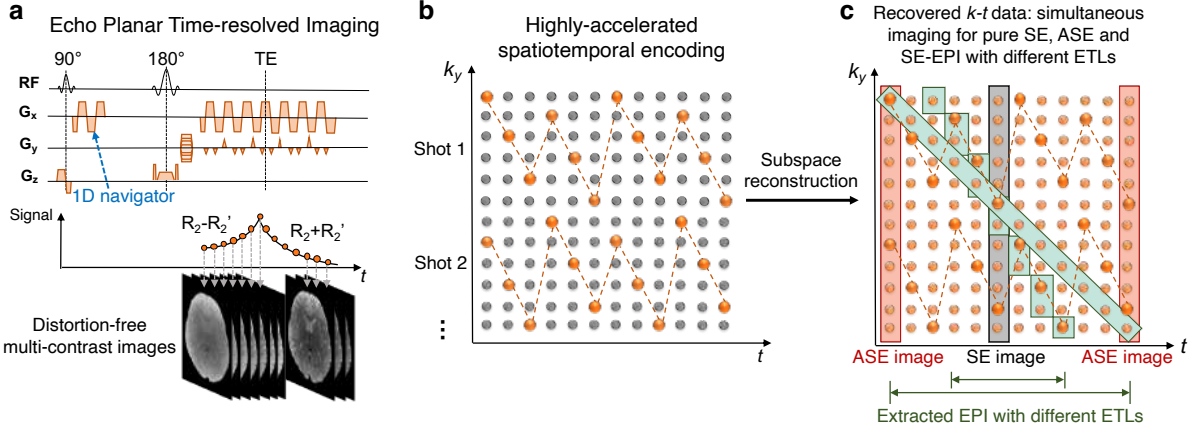
6 Conventional EPI acquires one phase encoding position per readout line through a fast continuous  
7 bipolar readout, and forms a single image by combining all of these signals acquired at different time points.  
8 Although its image contrast is mainly determined by the “effective” echo time (TE), the time when the  
9 central PE line is acquired, signal decay occurs across the sampling window and contrast weightings from  
10 other time points also contribute to the final image. For SE-EPI acquisition, the signal magnitude  $S(t)$  at  
11 time  $t$  after excitation in a mono-exponential model is:

$$12 \quad S(t) = \begin{cases} S(0)e^{-TE_{SE} \cdot R_2'} e^{-(R_2 - R_2')t} = S(0)e^{(t-TE_{SE}) \cdot R_2'} e^{-R_2 t} & t < TE_{SE} \\ S(0)e^{TE_{SE} \cdot R_2'} e^{-(R_2 + R_2')t} = S(0)e^{(TE_{SE}-t) \cdot R_2'} e^{-R_2 t} & t > TE_{SE} \end{cases}, \quad (1)$$

13 where  $S(0)$  represents the initial signal intensity at  $t = 0$ ,  $TE_{SE}$  is the echo time of the spin-echo,  $R_2$  is the  
14  $T_2$  relaxation rate,  $R_2' = R_2^* - R_2$ , representing the difference between  $T_2^*$  and  $T_2$  relaxation rates and  
15 reflecting the susceptibility-induced recoverable intra-voxel dephasing, which is sensitive to extravascular  
16 BOLD surrounding all vessels including large veins. As shown in the signal model, pure  $T_2$ -weighted signal  
17 can be obtained at  $TE_{SE}$ , while all the other time points will be affected by  $R_2'$ -weighting with an extent  
18 determined by the time interval between their acquisition time and the SE refocusing time. Signals acquired  
19 at those time points with  $R_2'$ -weighting will therefore induce contrast contamination in SE-EPI when they  
20 are combined to form an EPI image, leading to increased sensitivity to large vessels and compromised  
21 neuronal specificity.

22 The main concept of SE-EPTI is to recover a series of images across the readout at all those time points  
23 by recovering fully-sampled data across the  $k$ - $t$  space (Dong et al., 2021a; Dong et al., 2020; Dong et al.,  
24 2019; Wang et al., 2019; Wang et al., 2021a). Figure 1a shows the sequence diagram of SE-EPTI that is  
25 used to achieve this goal, where an EPI-like continuous readout is used in a SE acquisition with different  
26  $G_y$  gradient blips applied to sample a  $k_y$ -segment in  $k$ - $t$  space using a spatiotemporal CAIPI encoding pattern  
27 (Fig. 1b). This sampling pattern not only ensures that the neighboring  $k_y$  points are sampled within a short  
28 time interval with high temporal correlations, but also that they are interleaved and complementary along  
29 the  $k_y$  direction in an optimized pattern. It allows efficient use of temporal correlation and coil sensitivity  
30 to achieve high undersampling, therefore only a few EPTI shots are needed to cover the desired  $k$ - $t$  space  
31 for imaging. After the full  $k$ - $t$  space is recovered in the reconstruction, multi-contrast images with pure  
32 contrast at all time points can be simply obtained by an inverse Fourier transform, including a pure  $T_2$  SE

1 image and a series of ASE images with varying  $T_2'$  weighting, spaced at a TE increment of an echo-spacing  
 2 ( $\sim 1$  ms) as shown in Fig. 1b. These images are free from any distortion and blurring artifacts, which are  
 3 common in conventional EPI due to  $B_0$ -inhomogeneity-induced phase accumulation and signal decay across  
 4 the readout. This is because each EPTI image is recovered using signals with exactly the same phase and  
 5 magnitude.



6 **Figure 1.** Spatiotemporal CAIPI encoding of EPTI and generation of multi-contrast images. The recovered  
 7  $k\text{-}t$  data after reconstruction can provide SE image with pure  $T_2$  weighting (gray), asymmetric SE (ASE)  
 8 images with both  $T_2$  and  $T_2'$  weighting (orange), and extracted SE-EPI with different ETLs (green) to  
 9 investigate the effect of  $T_2'$  contamination.  
 10

## 11 2.2. EPTI-extracted conventional EPI with different echo train lengths

12 In conventional SE-EPI acquisition, the reduction of ETL can help reduce the level of  $R_2'$   
 13 contamination, which can be achieved through in-plane acceleration using parallel imaging and/or through  
 14 multi-shot segmentation. However, a large reduction factor in ETL would lead to either large noise  
 15 amplification and aliasing artifacts in parallel imaging and/or a long acquisition time in multi-shot  
 16 acquisition. Therefore, it remains challenging to achieve short ETLs for SE-EPI especially at high spatial  
 17 resolution.

18 To investigate the benefit of reducing  $T_2'$  contamination by using a shorter ETL as well as comparing  
 19 the conventional SE-EPI with the pure SE images, data that are equivalent to a conventional EPI-like  
 20 acquisition with different ETLs can be extracted from the reconstructed  $k\text{-}t$  data acquired by EPTI. Fig. 1c  
 21 shows a simplified illustration of such extraction, where reconstructed  $k\text{-}t$  signals at different time  
 22 points or TEs are extracted in a diagonal pattern in  $k\text{-}t$  space. To mimic an interleaved ms-EPI acquisition,  
 23 multiple adjacent PE lines are extracted at each time point depending on the shot number (e.g., 4 PE lines  
 24 for a 4-shot EPI), and the final ETL of the extracted SE ms-EPI is determined by the overall matrix size  
 25 along PE direction as well as the shot number. For example, for a 4-shot EPI acquisition with a matrix size  
 26 of 144, 4 PE lines are extracted at each time point, and the resultant ETL will be 36. Before the extraction,

1  $B_0$ -induced phase is removed from the  $k$ - $t$  data by removing the TE-dependent linear phase changes in the  
2 image domain, so that the EPTI-extracted SE-EPI images are also free from any distortion. This ensures  
3 that all the image contrasts obtained concurrently from a single EPTI dataset, including the pure SE, the  
4 ASE series and the extracted SE-EPI, are geometrically matched, allowing for reliable evaluation of the  
5 impact of  $T_2'$  contamination with different ETLs on the signal contributions.

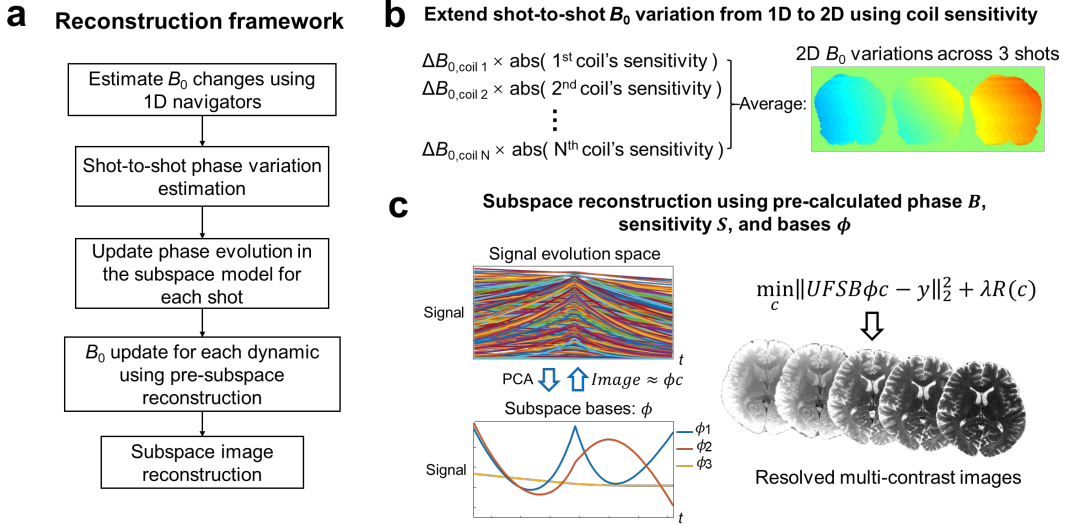
6 *2.3. Subspace image reconstruction*

7 The reconstruction framework of EPTI used in this study is shown in Fig. 2. To reconstruct the image  
8 series from the undersampled  $k$ - $t$  data, a low-rank subspace method (Dong et al., 2020; Guo et al., 2021;  
9 He et al., 2016; Lam and Liang, 2014; Liang, 2007; Meng et al., 2021; Tamir et al., 2017) is applied to  
10 resolve signal evolutions across different TEs using signal model priors (Fig. 2c). Here, the reconstruction  
11 is performed to estimate a small number of coefficient maps of pre-calculated temporal subspace bases that  
12 can accurately represent the signal evolution across echoes, rather than to estimate all of the echo images  
13 directly. Such a reconstruction approach can achieve improved reconstruction conditioning and good  
14 reconstruction accuracy by taking advantage of the high spatiotemporal correlation in the EPTI datasets. In  
15 this work, we tailor this subspace reconstruction specifically to the SE-EPTI acquisition and further  
16 incorporate corrections for phase variations due to  $B_0$  changes across different shots and dynamics,  
17 increasing the robustness and accuracy of the reconstruction for fMRI experiments.

18 In the reconstruction, the first step is to use principal component analysis (PCA) to generate a group  
19 of subspace bases  $\phi$  from simulated signal evolutions across a range of possible  $T_2$  and  $T_2^*$  values. The  
20 number of bases is selected to approximate all the simulated signal evolutions accurately with an error of  
21 <0.2% (3 bases in this work). Then, the coefficient map of the basis,  $c$ , is estimated by:

$$22 \min_c \|UFSB\phi c - y\|_2^2 + \lambda R(c), \quad (2)$$

23 Here,  $B$  is the image phase evolutions across echoes caused by field inhomogeneity,  $S$  is the sensitivity map,  
24  $F$  denotes the Fourier transform,  $U$  represents an undersampling mask, and  $y$  is the acquired undersampled  
25 data.  $R$  is the locally low-rank (LLR) constraint applied on the coefficients to further improve the  
26 conditioning, and  $\lambda$  is the control parameter. The image phase evolution  $B$  and coil sensitivity  $S$  are  
27 estimated from a low-resolution  $k$ - $t$  calibration scan acquired prior to the imaging scan. After estimating  
28 the coefficients, multi-contrast echo images can be recovered by performing a temporal expansion ( $\phi c$ ) for  
29 all the TEs in each volume TR.



1  
2 **Figure 2.** (a) EPTI reconstruction framework with dynamic  $B_0$  correction and shot-to-shot phase variation  
3 correction. (b) Illustration of the estimation method for shot-to-shot  $B_0$  variation using multi-channel 1D  
4 navigators. (c) Subspace reconstruction to resolve multi-contrast images by solving a small number of  
5 coefficient maps of the subspace bases.

6 *2.4. Shot-to-shot phase variation correction using navigator*

7 The  $B_0$ -inhomogeneity-induced phase accumulation could change temporally due to  $B_0$  drift and/or  
8 respiratory motion. Instead of inducing aliasing artifacts as in the conventional interleaved ms-EPI, such  
9 phase variations were shown to only cause minor local image smoothing on EPTI images due to the  $k_y$   
10 block-segmented sampling pattern used (Wang et al., 2019). To mitigate these smoothing effects and  
11 improve the reconstruction accuracy, a method to estimate and correct for such shot-to-shot phase variations  
12 is incorporated into the reconstruction framework as shown in Fig. 2.

13 One dimensional (1D)  $B_0$  changes along  $x$  between all of the EPTI-shots and temporal dynamics are  
14 calculated first. Specifically, the phases of the 1<sup>st</sup> and 3<sup>rd</sup> echo of the standard 3-line EPI phase correction  
15 navigator (acquired after the excitation pulse but before the refocusing) are subtracted and scaled based on  
16 their TEs to obtain the  $B_0$  of every TR, and then the relative  $B_0$  changes to the first TR are calculated. The  
17 1<sup>st</sup> and 3<sup>rd</sup> echo are used in this calculation to avoid odd-even echo phase difference in the bipolar readout.  
18 These 1D  $B_0$  changes are then extended to 2D by using the spatial information provided by the multi-  
19 channel coil sensitivities (Splitthoff and Zaitsev, 2009; Versluis et al., 2012; Wallace et al., 2020). Since the  
20 shot-to-shot  $B_0$  change varies smoothly in the spatial domain, the low-frequency spatial information  
21 provided by the multi-channel coils should be sufficient in capturing and recovering its spatial distribution  
22 along the PE direction. Specifically, the 2D  $B_0$  change,  $\Delta B_{2D}$ , can be approximated by a weighted  
23 combination of the 1D  $B_0$  changes from different coils using the magnitude of their coil sensitivities, similar  
24 to a previous approach (Versluis et al., 2012). The estimation process is as follows:

$$1 \quad \Delta B_{2D} = \frac{1}{N} \sum_{i=1}^N \Delta B_{1D,i} |S_i|, \quad (3)$$

2 where  $\Delta B_{1D,i}$  is the 1D  $B_0$  change estimated from the  $i$ -th coil, and  $|S_i|$  is the magnitude of the  $i$ -th coil's  
 3 sensitivity map. Next, to correct for the shot-to-shot  $B_0$  changes in the reconstruction, the phase evolution  
 4 term  $B$  in Eq. 2 is updated to incorporate the above estimated  $B_0$ -induced phase into the forward model. A  
 5 simulation experiment was performed to evaluate the effectiveness of the above shot-to-shot phase variation  
 6 correction approach. The simulated data were generated using the imaging parameters and a set of  
 7 quantitative maps ( $T_2$ ,  $T_2^*$ ,  $B_0$  map) obtained from EPTI data in the in-vivo experiments, with additional  
 8 smooth  $B_0$  changes (spatially 2<sup>nd</sup> order) added to each shot as described below.

9 To account for higher-order  $B_0$  spatial changes, a pre-reconstruction process is also implemented to  
 10 update the  $B_0$  maps across different dynamics. It uses pre-reconstructed 2D phase maps to help better  
 11 estimate higher-frequency spatial variations of  $B_0$  changes, which can be used to adjust the forward model  
 12 to improve the final reconstruction accuracy. In the  $B_0$  update pre-reconstruction, a set of complex subspace  
 13 bases are first extracted from simulated signals with a range of  $B_0$  changes, which are then used in the pre-  
 14 reconstruction model to estimate higher order phase evolution and  $B_0$ . The estimated  $B_0$  changes are filtered  
 15 by a hamming filter to remove any noise and potential artifacts, and then incorporated into the final image  
 16 reconstruction by updating the phase term  $B$  (Eq. 2), similar to the approach described in (Dong et al.,  
 17 2021a). More number of bases were used in the  $B_0$  update pre-reconstruction than in the image  
 18 reconstruction (6 complex bases vs. 3 real bases) to provide additional degrees of freedom to model and  
 19 estimate large  $B_0$  phase evolution.

20 *2.5. Data acquisition*

21 Written informed consent was obtained from each participant before the experiment in accordance  
 22 with our institution's Human Research Committee. All data were acquired on a Siemens Magnetom Terra  
 23 7T scanner (Siemens Healthineers, Erlangen, Germany), using a custom-built 64-channel receiver coil  
 24 (Mareyam et al., 2020) with a single RF transmission channel.

25 SE-EPTI data were acquired on 3 healthy volunteers using the following acquisition parameters: FOV  
 26 =  $218 \times 130 \times 25.2$  (RO  $\times$  PE  $\times$  slice, HF-LR-AP) mm<sup>3</sup>, matrix size =  $240 \times 144 \times 28$ , 0.9-mm isotropic  
 27 resolution, number of EPTI-shots (segmentation) = 3, number of echoes = 45, TE<sub>range</sub> = 40–88 ms, TE of  
 28 SE = 64 ms, echo spacing (TE-increment) = 1.09 ms, volume TR = 3 s  $\times$  3-shot = 9 s, 43 dynamics,  
 29 acquisition time per run = 6 min 27 s, 14 runs were acquired for each subject. A standard block-design  
 30 “checkerboard” visual stimulus contrast-reversing at 8 Hz was presented for the fMRI acquisitions. An  
 31 initial 27-s fixation period was performed followed by four 36 s-54 s on-and-off blocks. To assist with  
 32 fixation, a red dot with time-varying brightness was positioned at the center of the screen, and the subjects  
 33 were asked to press a button as soon as they detected a change in its brightness. Before the EPTI data

1 acquisition in each run, a fast  $k\text{-}t$  calibration scan was acquired in 54 s with a matrix size of  $240 \times 49 \times 28$   
2 (RO  $\times$  PE  $\times$  slice) and 7 echoes. For each volunteer, a multi-echo magnetization-prepared rapid gradient  
3 echo (MEMPRAGE) (van der Kouwe et al., 2008) image was acquired at 0.75-mm isotropic resolution as  
4 an anatomical reference with a FOV of  $= 218 \times 168 \times 194$  (AP-LR-HF) mm $^3$ .

5 Conventional single-shot SE-EPI and GE-EPI were also acquired for comparison on one of the healthy  
6 volunteers. The acquisition parameters for SE-EPI were: FOV =  $218 \times 130 \times 25.2$  (RO  $\times$  PE  $\times$  slice, HF-  
7 LR-AP) mm $^3$ , matrix size =  $240 \times 145 \times 28$ , 0.9-mm isotropic resolution, TE = 64 ms, GRAPPA factor =  
8 3, ETL = 52 ms, echo spacing = 1.09 ms, TR = 3 s. The GRAPPA factor of 3 was used here to allow the  
9 same TE to be achieved as the EPTI acquisition. The GE-EPI used the same FOV and resolution, and other  
10 acquisition parameters were: TE = 28 ms, GRAPPA factor = 4, ETL = 39 ms, echo spacing = 1.09 ms, TR  
11 = 3 s. Noted that a GRAPPA factor of 3 or 4 used here is already high, considering the small FOV along PE  
12 in our acquisition (i.e.,  $\sim 1.6x$  zoomed compared to standard axial scan with PE along AP). 129 dynamics  
13 were acquired per run for both GE- and SE-EPI in an acquisition time of 6 min 27 s. 4 runs were acquired  
14 for both GE- and SE-EPI. In order to estimate field maps and correct for geometric distortions, PE-reversed  
15 data were acquired for both GE- and SE-EPI with matched acquisition parameters prior to the fMRI  
16 acquisitions. The standard GRAPPA (Griswold et al., 2002) reconstruction was performed followed by  
17 complex coil combination (Pruessmann et al., 1999b). In addition, a turbo spin-echo (TSE) image was  
18 acquired with the same FOV and matrix size as a distortion-free reference.

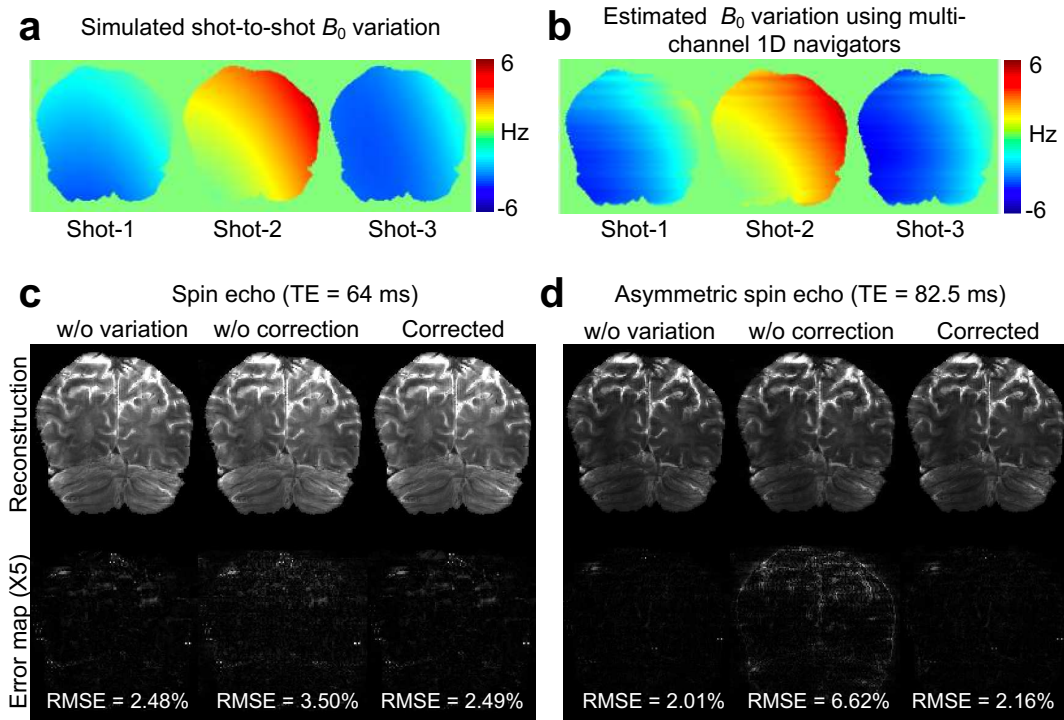
#### 19 2.6. *Image post-processing*

20 To align all the volumes from different dynamics and runs, registration was performed using AFNI  
21 (Cox, 1996). For EPTI, the motion parameters were estimated using the all-echo-averaged volumes with  
22 higher SNR, which were then applied to different multi-echo volumes as well as the extracted ms-EPI  
23 images. After registration, the multi-run data were averaged to a single dataset. For ss-EPI, distortion  
24 correction was performed using the  $B_0$  maps estimated from ‘topup’ (Andersson et al., 2003) using the pre-  
25 acquired PE-reversed data. The  $B_0$  maps were motion-corrected to account for the field map orientation  
26 change due to subject motion, and then applied to each volume using the ‘FUGUE’ function in FSL  
27 (Jenkinson et al., 2012; Smith et al., 2004).

28 For cortical surface-based analysis, cortical reconstructions were generated automatically using  
29 Freesurfer (Desikan et al., 2006; Fischl, 2012; Fischl et al., 2002) on the MPRAGE images of each subject.  
30 A total of 9 equi-volume (Waehnert et al., 2014; Waehnert et al., 2016) cortical layers were reconstructed,  
31 and applied to the EPTI and EPI data to investigate the distribution of the z-score and the percent signal  
32 change across different cortical depths.

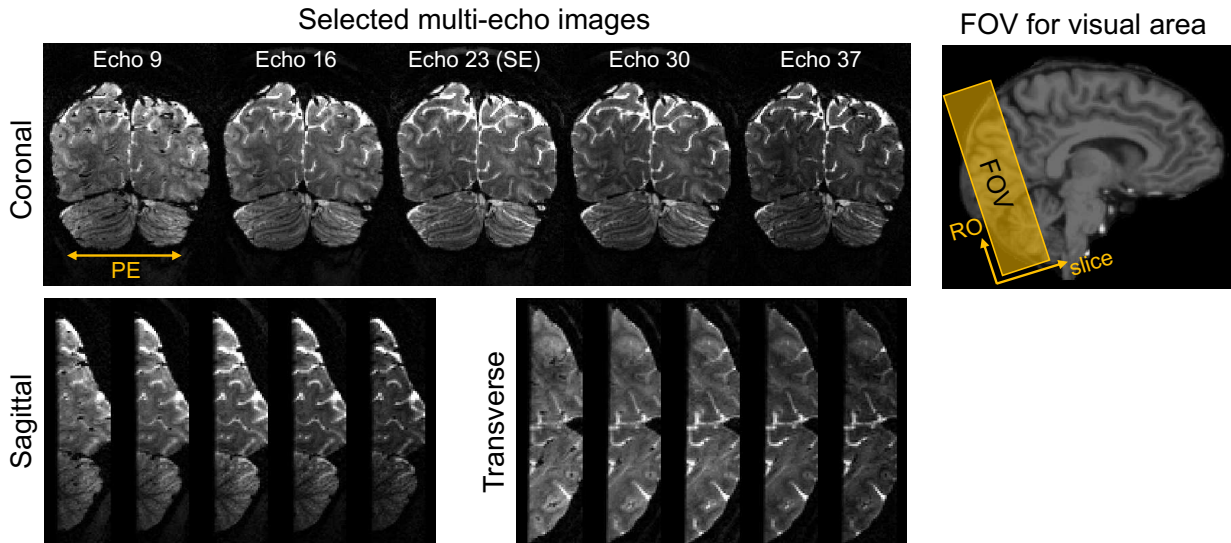
1 **3. Results**

2 The effect of the shot-to-shot phase variations on the EPTI reconstruction and the performance of the  
 3 estimation and correction methods are evaluated in Fig. 3. Large temporal  $B_0$  variations with a range of  $\pm 10$   
 4 Hz were used in this evaluation to simulate the effect at 7T. The estimated  $B_0$  variation maps (Fig. 3b) show  
 5 spatial distribution similar to the reference (Fig. 3a), demonstrating the effectiveness of the  $B_0$  variation  
 6 estimation method using multi-channel 1D navigators. The reconstructed images without and with  
 7 correction are compared and shown for the pure SE (Fig. 3c) and a selected ASE (Fig. 3d) image. The  
 8 images without any added variations are also shown in the left-most columns to illustrate baseline  
 9 reconstruction errors when compared to the ground truth simulated fully-sampled data. As shown in the  
 10 error maps, the pure SE image is less affected by the phase variations and presents with only a small increase  
 11 in RMSEs even without correction, while the ASE image shows higher errors resulted from the phase  
 12 variations due to its larger  $B_0$  phase accumulation. After correction, the errors are significantly mitigated,  
 13 especially for the ASE image, and similar reconstruction accuracy is observed as in the case without any  
 14 added phase variations, demonstrating the effectiveness of the proposed correction approach.

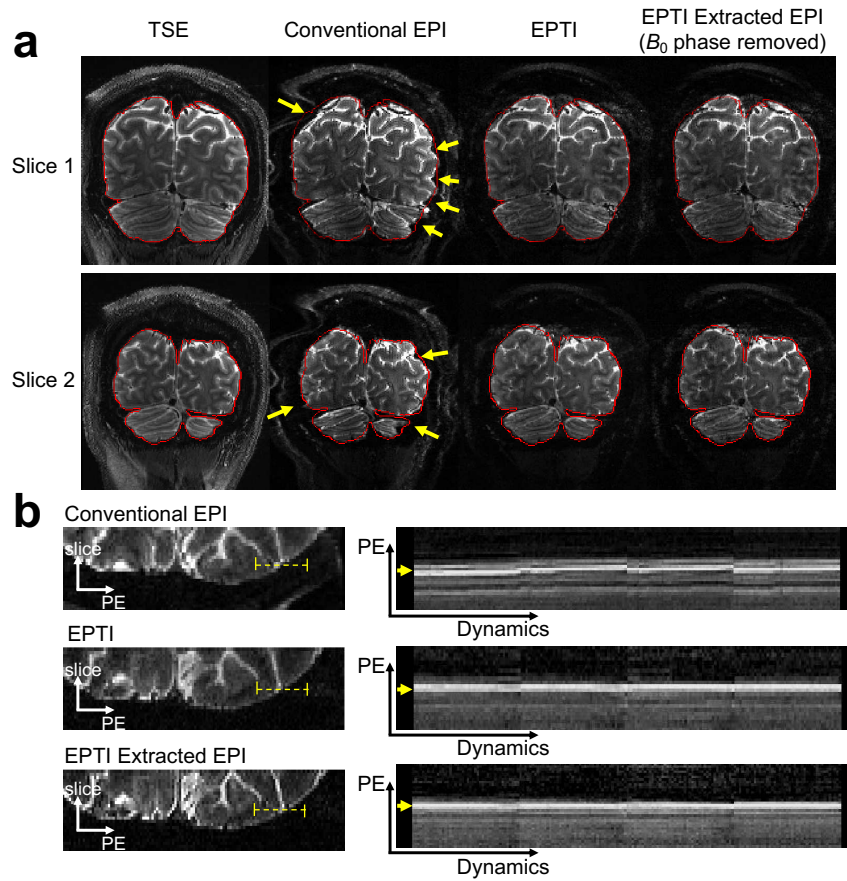


15  
 16 **Figure 3.** Evaluation of the shot-to-shot  $B_0$  variation estimation and correction method. (a) Simulated shot-  
 17 to-shot  $B_0$  variation maps of the 3-shot acquisition (spatially 2<sup>nd</sup> order). (b) Estimated  $B_0$  variation maps  
 18 using multi-channel 1D navigators. (c) Reconstructed pure SE images (TE = 64 ms) and their corresponding  
 19 error maps ( $\times 5$ ) without variations, with variations but without correction, and after correction. (d)  
 20 Reconstructed images and error maps for the ASE at TE = 82.5 ms. The RMSEs were listed at the bottom  
 21 of each error map.

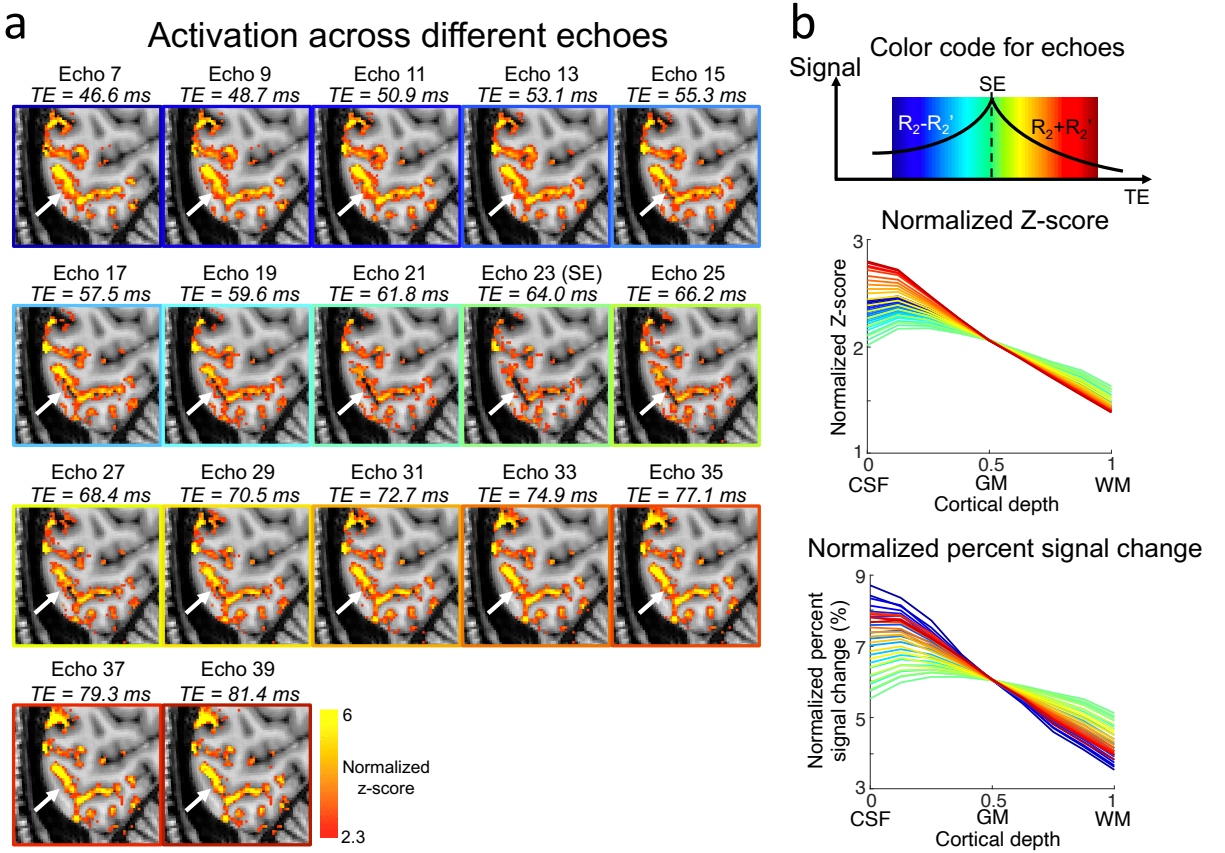
1       Figure 4 shows an example of the multi-echo images from a representative temporal dynamic acquired  
 2       by SE-EPTI in three orthogonal views, after averaging all the runs in the visual-task experiment at 7T. The  
 3       FOV of the acquisition was selected to cover the visual cortex as shown on the right. Figure 5a compares  
 4       the geometric distortion between conventional SE-EPI, EPTI and EPTI-extracted EPI. Two different slices  
 5       are presented with overlaid brain contours (red lines) extracted from the distortion-free TSE image collected  
 6       in the same scan session. The conventional EPI shows severe distortion at multiple areas highlighted by the  
 7       yellow arrows. In contrast, both EPTI and the EPTI-extracted EPI are free from such distortion artifacts  
 8       and provide identical contours as the TSE reference. Note that the EPTI-extracted EPI images were  
 9       generated after removing the  $B_0$  phase in the full  $k$ - $t$  data (not possible with conventional EPI data), therefore  
 10      are free from the geometric distortion, similar to the EPTI images. In addition, EPTI is also robust to  
 11      dynamic  $B_0$ /susceptibility changes, and provides images free from distortion changes across time as  
 12      demonstrated in Fig. 5b. As shown in the zoom-in 1D signal profile along the PE direction (extracted from  
 13      the locations indicated by the yellow dotted lines) across different dynamics and runs, conventional EPI  
 14      suffers from dynamic changes in distortion that are hard to correct for, while the signal profiles of EPTI and  
 15      EPTI-extracted EPI are almost static and consistent across time.



16  
 17      **Figure 4.** Examples of multi-echo EPTI images (left) acquired in the fMRI experiment covering the visual  
 18      cortex (right). The images are shown for each dynamic after averaging all the runs. Three orthogonal views  
 19      are presented for 5 selected echoes out of the total 45 echoes.



1  
2 **Figure 5.** (a) Distortion comparison between the TSE reference, conventional EPI, EPTI and EPTI-  
3 extracted EPI. The image contours extracted from the TSE image are applied to all images (red lines).  
4 Conventional EPI shows obvious distortions at multiple areas (yellow arrows), while EPTI and EPTI-  
5 extracted EPI have almost identical image contours with the TSE image. (b) Evaluation of dynamic  
6 distortion changes. The zoomed-in 1D PE profiles (extracted from the locations indicated by the yellow  
7 dotted lines on the left) across different dynamics and runs are shown on the right to compare the level of  
8 dynamic distortion in conventional EPI, EPTI and EPTI-extracted EPI.

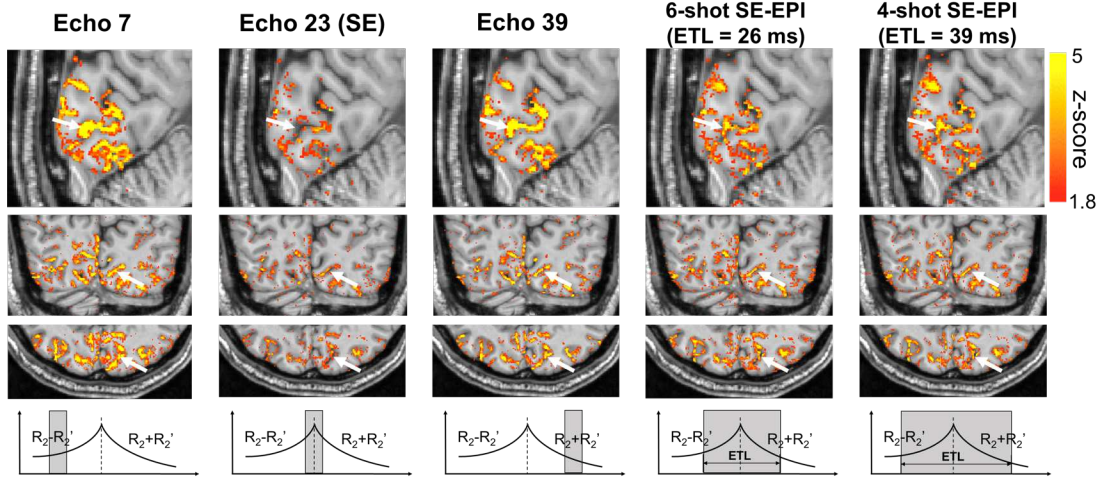


1

2 **Figure 6.** (a) Normalized z-score activation maps of different EPTI echo images. The white arrow shows  
3 an example region where the activation in the CSF is reduced relative to that in the gray matter in echoes  
4 with less  $T_2'$  contributions. Normalization was performed based on the sum of the positive z-scores of each  
5 echo to normalize the sensitivity differences and to better visualize activation pattern. (b) Cortical depth  
6 dependent profiles of z-score and percent signal change of all the echoes (color-coded by echo indices  
7 shown on the top) across V1. The profiles from different echoes are normalized to have the same value at  
8 0.5 cortical depth of the SE (echo 23) to better compare the slope difference.

9 The varying  $T_2'$  effect across the spin-echo readout was investigated using the time-resolved multi-  
10 echo EPTI images as shown in Fig. 6. Fig. 6a shows the activation maps within visual cortex across different  
11 echoes in normalized z-scores, where a scaling was performed across different echoes based on the sum of  
12 the positive z-scores of each echo to normalize their sensitivity difference and to better compare the  
13 activation patterns. As expected, with less  $T_2'$  contrast in the images closer to the pure spin-echo (from echo  
14 7 to echo 23, or from echo 39 backwards to echo 23), there is less activation in the CSF region (white  
15 arrows) compared to the activation in the gray matter, with the peak of the activation gradually shifting  
16 from centering in the CSF region towards the gray matter parenchyma on the side. This can also be seen in  
17 the cortical depth dependence analysis shown in Fig. 6b, where the cortical profiles of the z-score and the  
18 percent signal change across V1 of all the echoes (color-coded by echo indices, pure SE shown in green)

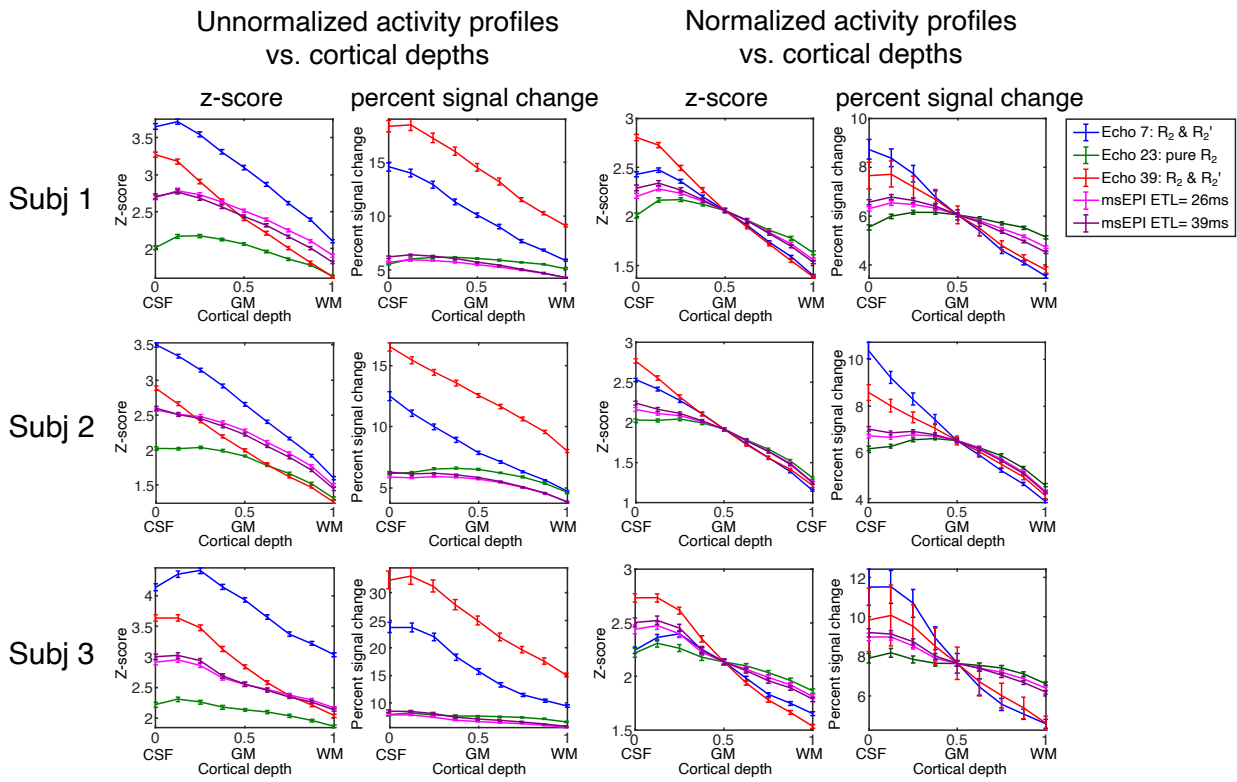
1 are plotted. The profiles from different echoes were scaled to have the same value at 0.5 cortical depth as  
 2 the SE (echo 23) to better compare the difference in slope. The first few echoes in blue with large amount  
 3 of  $T_2'$  weightings exhibit the expected bias to large veins, manifesting as depth profiles that peak at the pial  
 4 surface. As TE increases and moves closer to the SE from blue to green, lower and lower pial surface bias  
 5 were observed in flatter depth profiles with lower values at the pial surface. At the SE position (pure  $T_2$ ),  
 6 the smallest slope with minimal bias is observed. Then, as TE moves away from the SE position with more  
 7  $T_2'$  weighting, the pial vessel bias returns and the slope increases. In summary, the slope of these cortical  
 8 profiles or the amount of large vessel bias across echoes show good correspondence to the amount of  $T_2'$   
 9 weighting in the theoretical signal model (Eq. 1), both of which are lowest at SE, and increase with the  
 10 distance away from SE. This observation suggests that, by experimentally reducing  $T_2'$  weighting in the  
 11 image, the macrovascular effects can be effectively reduced. It also demonstrates that EPTI provides a  
 12 powerful tool to resolve all these multi-contrast images across the EPTI readout, and to investigate gradual  
 13 TE-dependent BOLD signal change at a TE increment as short as 1 ms using data acquired in a single scan.



14  
 15 **Figure 7.** Comparison of activation in unnormalized z-score between ASE images, pure SE image, and  
 16 extracted SE-EPI all obtained from EPTI. The pure SE image shows lower sensitivity than ASE echoes and  
 17 the conventional SE-EPI, but despite the sensitivity difference, we can still observe that the peak of the  
 18 activation map itself is more in the gray matter regions rather than centered in the CSF as indicated by the  
 19 white arrows.

20 Figure 7 compares unnormalized activation maps (z-score) calculated from EPTI ASEs (echo 7 and  
 21 39), EPTI pure SE (echo 23), and two EPTI-extracted SE ms-EPI with ETLs of 26 ms (6-shot) and 39 ms  
 22 (4-shot). The ASE images with large  $T_2'$  weightings show high activation in both the CSF and gray matter  
 23 areas. The pure SE image and the extracted SE-EPI images show overall less activations as expected due  
 24 to the reduced activation sensitivity of  $T_2$  contrast. Despite such a sensitivity difference, it can still be  
 25 observed that the three cases of  $T_2$  images, including the pure SE and the two extracted SE-EPI images,  
 26 show a reduction of activation in the CSF areas when compared to the gray matter's activation level in the

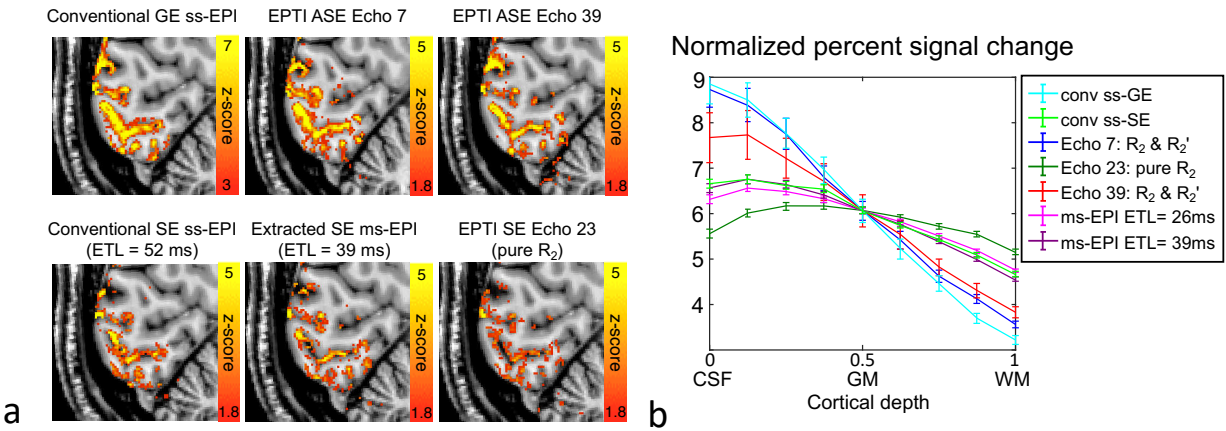
1 same maps. The pure SE image shows minimal CSF bias, pointing to EPTI's ability to provide a more pure  
 2 SE contrast with further reduction in  $T_2'$  contamination compared to the conventional ms-EPI, and achieve  
 3 higher microvascular specificity. The cortical depth analysis of these five cases in 3 healthy volunteers are  
 4 shown in Fig. 8. Both the unnormalized and normalized activity profiles are plotted. The unnormalized  
 5 profiles demonstrate the sensitivity differences between  $T_2'$  and  $T_2$  weighted BOLD contrasts as previously  
 6 described above, while the normalized profiles better compare the amount of large vessel bias through their  
 7 slope differences. Consistent with the results in Fig. 6 and 7, the data from all the three subjects show that  
 8 the pure SE image (echo 23, dark green) achieves the lowest slope and minimal macrovascular bias  
 9 compared to the ASE images and the extracted conventional SE ms-EPI. In addition, the results also confirm  
 10 that the conventional SE ms-EPI with a longer ETL will have larger pial vessel bias (Fig. 8, light and dark  
 11 purple lines).



12  
 13 **Figure 8.** Cortical-depth profiles of the unnormalized (left two columns) and normalized (right two columns)  
 14 z-score and percent signal change in three subjects ( $N = 3$ ). Five EPTI data are compared in each plot,  
 15 including selected ASE images (echo 7 and 39), pure SE image (echo 23), extracted SE ms-EPI with ETL  
 16 = 26 ms (6 shots) and 39 ms (4 shots). In all three subjects, the pure SE image shows the lowest slope with  
 17 decreased activation at the CSF-GM interface, indicating a reduced level of bias from large veins.

18 Further confirmation is provided by the comparison between the EPTI acquired images and the actual  
 19 acquired in-plane accelerated single-shot GE and SE EPI as shown in Fig. 9. The ASE EPTI images (Echo

7 and 39) show consistent activation localization to the conventional GE-EPI, with high level of activation in both CSF and gray matter due to their large  $T_2'$  weighting. The cortical profile of the conventional GE-EPI also exhibits large vessel bias near the pial surface similar to the ASE EPTI images (light blue vs. dark blue or red). The conventional SE-EPI shows a reduced sensitivity to large vessels when compared to the GE/ASE acquisitions, but still has a higher activation in the CSF and a higher slope (Fig. 9a bottom row, left-most column and Fig. 9b light green) when compared to the pure SE EPTI image (Fig. 9a bottom row, right-most column and Fig. 9b dark green). This result further demonstrates the reduced draining vein effects in the pure SE EPTI image over conventional SE-EPI image. The conventional SE ss-EPI (with a GRAPPA factor of 3) also shows similar activation to the extracted SE ms-EPI with similar macrovascular bias. Noted that the conventional images were acquired in a different session than EPTI data and could have potential residual distortion after correction, which might introduce bias when comparing them with EPTI data.



13  
14 **Figure 9.** (a) Comparison between activation maps of the conventional GE-EPI, SE-EPI, and EPTI images.  
15 The ASE EPTI images (echo 7 and 39) with  $T_2'$  weighting show similar activation localization as the  
16 conventional GE-EPI, while the pure SE EPTI image (echo 23) provides less bias in CSF than the  
17 conventional SE-EPI. (b) Comparison of the cortical-depth profiles between the acquired GE-EPI, SE-EPI,  
18 selected EPTI echo images and EPTI-extracted EPIS with different ETLs.

#### 19 4. Discussion and conclusions

20 The visual-task experiments in this study preliminarily demonstrate the ability of EPTI to time-resolve  
21 multi-echo images at a small TE increment to investigate the varying  $T_2'$  weighting across the spin-echo  
22 readout. The observed gradual reduction of large vein bias in image echoes closer to SE with less and less  
23  $T_2'$  weighting confirms the expected association between  $T_2'$  contrast and the macrovascular bias. Moreover,  
24 the pure SE image acquired by EPTI shows reduced macrovascular bias compared with both the EPTI-  
25 extracted SE-EPI and the acquired conventional SE-EPI acquisition, indicating that EPTI exhibits reduced  
26  $T_2'$  weighting and a purer  $T_2$  BOLD contrast over conventional EPI (even with multiple shots) for improved

1 microvascular specificity. We have also experimentally confirmed that a longer ETL in SE-EPI will  
2 introduce more macrovascular bias in human experiments, consistent with the result of the previous study  
3 conducted in Monkey V1 (Goense and Logothetis, 2006). The ability of EPTI to simultaneously acquire  
4 multi-contrast images in a single scan provides a powerful tool to examine the microvascular and  
5 macrovascular contribution in  $T_2$  and  $T_2'$  BOLD contrasts. This helps to avoid any confounding differences  
6 in activation that occur between scans that would be possible in sequentially acquired runs. The similar  
7 level and consistent localization of activation seen in the EPTI ASEs data and in the GE-EPI data, and as  
8 well as between the EPTI-extracted SE-EPI data and the actual SE-EPI data (Fig. 9), demonstrates the  
9 reliability of these multi-contrast images generated from a single EPTI dataset.

10 In this study, we focus on investigating the reduced macrovascular contribution and improved  
11 microvascular specificity using the pure  $T_2$  BOLD provided by EPTI. The multi-echo images with varying  
12  $T_2'$  and  $T_2$  BOLD contrasts, which provide varying levels of both macrovascular-sensitivity and  
13 microvascular-specificity, could also be combined to potentially allow joint modeling to improve both the  
14 sensitivity and specificity to detect neuronal activation using BOLD contrast. The multi-echo images can  
15 also be used to enhance the CNR of BOLD (Poser et al., 2006; Posse et al., 1999) or to remove physiological  
16 noise through multi-echo denoising algorithms (Kundu et al., 2012; Kundu et al., 2017; Posse et al., 1999).  
17 Moreover, while our study uses a relative long  $TE_{SE}$  (64 ms) for the EPTI acquisition to allow for extraction  
18 of the conventional EPI data with different ETLs from the same dataset for comparison, the unique time-  
19 resolved imaging approach grants the flexibility to shift the echo train to achieve shorter TEs (Wang et al.,  
20 2021b), which could be particularly useful for investigating TE-dependent signal contributions in SE-  
21 BOLD, such as varying levels of extravascular and intravascular signal changes.

22 Another advantage of EPTI we presented in this study is that it eliminates the geometric distortion that  
23 is common in conventional EPI-based methods due to field inhomogeneity (Fig. 5a), which is more severe  
24 at ultra-high field and in high-resolution scans. Although post-processing methods have been developed  
25 and widely used to correct the distortion, using a field map or a pair of PE-reversed acquisition, the  
26 correction for dynamic changes in distortions due to susceptibility changes resulted from multiple sources  
27 such as head motion, system drift, and respiration still remains challenging, resulting in voxels  
28 displacements between dynamics or runs and affecting the reliability of the fMRI results. In the analysis,  
29 we have performed distortion correction of conventional EPI data using field maps calculated from pairs of  
30 PE-reversed images acquired before fMRI data acquisition, and we have also accounted for the orientation  
31 change of the field map due to subject movements. However, remaining distortion changes along the PE  
32 direction are still present across different dynamics in the time-series (Fig. 5b), resulting from susceptibility  
33 and field map changes within the scan that are hard to correct using pre-scanned field maps. This can  
34 degrade the subsequent fMRI analysis. EPTI removes the geometric distortion and dynamic distortion

1 changes through its time-resolving approach, where each echo image is formed using the data acquired at  
2 the exact same echo time (same  $B_0$  phase). The distortion-free images should help with registration to the  
3 anatomical data and lead to smaller errors in the cortical depth assignment. In addition, the time-resolving  
4 approach can also eliminate the image blurring along PE direction due to signal decay, another major  
5 limitation of conventional EPI.

6 Instead of geometric distortion in conventional EPI, the  $B_0$  change might lead to local blurring and  
7 elevated reconstruction errors in EPTI data as reported in our previous work (Wang et al., 2019). Here, we  
8 first characterized the impact of shot-to-shot phase variations or  $B_0$  changes on the multi-echo EPTI images.  
9 As expected, it was observed that the ASE images with more  $B_0$  phase accumulation are more sensitive to  
10 inter-shot variations than the pure SE image. To correct for this, the proposed reconstruction framework  
11 utilizes a navigator-based shot-to-shot  $B_0$  variation estimation that provides effective correction and  
12 significantly mitigates the potential blurring. A pre-reconstruction process was also incorporated to correct  
13 for higher-order  $B_0$  changes across dynamics that can further improve the reconstruction robustness.

14 By using the pure SE EPTI image, the cortical depth profiles of z-score and percent signal change  
15 show minimal pial surface bias. However, small amount of activation or bias was still observed within CSF  
16 or around pial surface. First, due to the use of the temporal correlation across echoes to reconstruct the  
17 highly-undersampled  $k$ - $t$  data, we do not rule out the possibility that there might be some  $T_2'$  contrast  
18 leakage and therefore residual pial surface bias in the pure SE EPTI image. Our original work on EPTI used  
19 a GRAPPA-like reconstruction in the  $k$ - $t$  space to reconstruct the images. The GRAPPA kernel interpolation  
20 along  $t$  could cause local temporal smoothing with an effective ETL estimated at  $\sim 7$  ms. This could cause  
21 small amount of  $T_2'$  contamination in the pure SE image, but is still within the range of ETLs that would  
22 provide microvasculature-dominated BOLD (Goense and Logothetis, 2006). In this work, a subspace  
23 reconstruction was employed to take advantages of the signal model prior that can accurately represent the  
24 signal evolution (errors  $< 0.2\%$ ), without interpolating along  $t$  as in the GRAPPA reconstruction, which  
25 should result in reduced amount of  $T_2'$  leakage and provide purer SE. To systematically characterize the  
26 potential residual  $T_2'$  contamination/leakage in the subspace reconstruction, a generalized approach to  
27 analyze the signal response of non-linear reconstruction (e.g., LLR-constraint subspace reconstruction in  
28 this work) might be required in the future. Second, partial volume effects and potential residual  
29 intravascular signal contribution (longer intravascular  $T_2$  than expected) could also be possible explanations.  
30 Biophysical modeling and simulation as well as experiments with different SE TEs (Berman et al., 2021;  
31 Pfaffenrot et al., 2021; Pflugfelder et al., 2011) should be helpful to better understand the signal  
32 contributions of SE BOLD fMRI.

33 At the current resolution, slightly higher activation can already be observed around the middle depth  
34 in the visual cortex, which might reflect higher microvascular density. However, the profiles are still

1 relatively flat across depths that could possibly be explained by an averaging effect over the large V1 ROI  
2 and/or by partial volume effects (De Martino et al., 2013; Koopmans et al., 2011). Further increases in  
3 spatial resolution can help reduce partial volume effect and should provide better visualization of such  
4 laminar fMRI responses. Recent laminar fMRI studies have also shown different responses in different  
5 layers in the motor cortex (Huber et al., 2017a), which may be useful to further evaluate the EPTI approach.  
6 The temporal resolution of EPTI acquisition could also be improved to increase the statistical power of  
7 fMRI analysis. These can be achieved by further developments of our EPTI-fMRI method to enable faster  
8  $k$ - $t$  encoding, such as by incorporating low-rank modelling across the fMRI time-series (Chiew et al., 2015),  
9 utilizing more advanced  $k$ - $t$  sampling trajectories (Dong et al., 2021b; Fair et al., 2020) or combining with  
10 multi-slice or multi-slab acquisition (Han et al., 2020; Setsompop et al., 2018; Setsompop et al., 2012),  
11 which will then open up an exciting opportunity to perform pure SE-fMRI at higher spatiotemporal  
12 resolution and larger spatial coverage.

13 **Acknowledgment**

14 This work was supported by the NIH NIBIB (R01-EB020613, R01-EB019437, R01-EB016695, P41-  
15 EB030006, and U01-EB025162) and NIHM (R01-MH116173) and made possible by resources provided  
16 by Shared Instrumentation Grants S10-OD023637, S10-OD02363701, S10-RR023401, S10-RR023043,  
17 and S10-RR019307. We thank Azma Mareyam for providing the 64-channel phased-array coil used in this  
18 study.

## 1 References

2 Andersson, J.L.R., Skare, S., Ashburner, J., 2003. How to correct susceptibility distortions in spin-echo  
3 echo-planar images: application to diffusion tensor imaging. *Neuroimage* 20, 870-888.

4 Bandettini, P.A., Wong, E.C., 1995. Effects of biophysical and physiologic parameters on brain  
5 activation-induced R2\* and R2 changes: simulations using a deterministic diffusion model. *Int. J. Imaging  
6 Syst. Technol.* 6, 133-152.

7 Bandettini, P.A., Wong, E.C., Hinks, R.S., Tikofsky, R.S., Hyde, J.S., 1992. Time course EPI of human  
8 brain function during task activation. *Magn. Reson. Med.* 25, 390-397.

9 Bandettini, P.A., Wong, E.C., Jesmanowicz, A., Hinks, R.S., Hyde, J.S., 1994. Spin-echo and gradient-  
10 echo EPI of human brain activation using BOLD contrast: a comparative study at 1.5 T. *NMR Biomed.* 7,  
11 12-20.

12 Barth, M., Meyer, H., Kannengiesser, S.A., Polimeni, J.R., Wald, L.L., Norris, D.G., 2010. T2-  
13 weighted 3D fMRI using S2-SSFP at 7 tesla. *Magn. Reson. Med.* 63, 1015-1020.

14 Beckett, A.J., Dadakova, T., Townsend, J., Huber, L., Park, S., Feinberg, D.A., 2020. Comparison of  
15 BOLD and CBV using 3D EPI and 3D GRASE for cortical layer functional MRI at 7 T. *Magn. Reson. Med.*  
16 84, 3128-3145.

17 Berman, A., Wang, F., Setsompop, K., Chen, J.J., Polimeni, J., 2021. Biophysical simulations of the  
18 BOLD fMRI signal using realistic imaging gradients: Understanding macrovascular contamination in Spin-  
19 Echo EPI. *Proc. Intl. Soc. Mag. Reson. Med.*, p. 3398.

20 Birn, R., Bandettini, P., 2002. The effect of T2'changes on spin-echo EPI-derived brain activation  
21 maps. *Proc. Intl. Soc. Mag. Reson. Med.*, Honolulu, 1324.

22 Bowen, C., Menon, R., Gati, J., 2005. High field balanced-SSFP fMRI: a BOLD technique with  
23 excellent tissue sensitivity and superior large vessel suppression. *Proc. Intl. Soc. Mag. Reson. Med.*, 119.

24 Boxerman, J.L., Hamberg, L.M., Rosen, B.R., Weisskoff, R.M., 1995. MR contrast due to  
25 intravascular magnetic susceptibility perturbations. *Magn. Reson. Med.* 34, 555-566.

26 Butts, K., de Crespigny, A., Pauly, J.M., Moseley, M., 1996. Diffusion-weighted interleaved echo-  
27 planar imaging with a pair of orthogonal navigator echoes. *Magn. Reson. Med.* 35, 763-770.

28 Chai, Y., Li, L., Huber, L., Poser, B.A., Bandettini, P.A., 2020. Integrated VASO and perfusion contrast:  
29 A new tool for laminar functional MRI. *Neuroimage* 207, 116358.

30 Chamberlain, R., Park, J.Y., Corum, C., Yacoub, E., Ugurbil, K., Jack Jr, C.R., Garwood, M., 2007.  
31 RASER: a new ultrafast magnetic resonance imaging method. *Magn. Reson. Med.* 58, 794-799.

32 Chen, N.-k., Guidon, A., Chang, H.-C., Song, A.W., 2013. A robust multi-shot scan strategy for high-  
33 resolution diffusion weighted MRI enabled by multiplexed sensitivity-encoding (MUSE). *Neuroimage* 72,  
34 41-47.

35 Chiew, M., Smith, S.M., Koopmans, P.J., Graedel, N.N., Blumensath, T., Miller, K.L., 2015. k-t  
36 FASTER: Acceleration of functional MRI data acquisition using low rank constraints. *Magn. Reson. Med.*  
37 74, 353-364.

38 Constable, R.T., Kennan, R.P., Puce, A., McCarthy, G., Gore, J.C., 1994. Functional NMR imaging  
39 using fast spin echo at 1.5 T. *Magn. Reson. Med.* 31, 686-690.

40 Cox, R.W., 1996. AFNI: software for analysis and visualization of functional magnetic resonance  
41 neuroimages. *Comput. Biomed. Res.* 29, 162-173.

42 De Martino, F., Yacoub, E., Kemper, V., Moerel, M., Uludağ, K., De Weerd, P., Ugurbil, K., Goebel,  
43 R., Formisano, E., 2018. The impact of ultra-high field MRI on cognitive and computational neuroimaging.  
44 *Neuroimage* 168, 366-382.

45 De Martino, F., Zimmermann, J., Muckli, L., Ugurbil, K., Yacoub, E., Goebel, R., 2013. Cortical depth  
46 dependent functional responses in humans at 7T: improved specificity with 3D GRASE. *PloS one* 8, e60514.

47 Denolin, V., Metens, T., 2003. Three-dimensional BOLD fMRI with spin-echo characteristics using  
48 T2 magnetization preparation and echo-planar readouts. *Magn. Reson. Med.* 50, 132-144.

49 Desikan, R.S., Ségonne, F., Fischl, B., Quinn, B.T., Dickerson, B.C., Blacker, D., Buckner, R.L., Dale,  
50 A.M., Maguire, R.P., Hyman, B.T., 2006. An automated labeling system for subdividing the human cerebral

1 cortex on MRI scans into gyral based regions of interest. *Neuroimage* 31, 968-980.

2 Dong, Z., Wang, F., Chan, K.S., Reese, T.G., Bilgic, B., Marques, J.P., Setsompop, K., 2021a. Variable  
3 flip angle echo planar time-resolved imaging (vFA-EPTI) for fast high-resolution gradient echo myelin  
4 water imaging. *Neuroimage* 232, 117897.

5 Dong, Z., Wang, F., Ma, X., Zhang, Z., Dai, E., Yuan, C., Guo, H., 2018. Interleaved EPI diffusion  
6 imaging using SPIR i T-based reconstruction with virtual coil compression. *Magn. Reson. Med.* 79, 1525-  
7 1531.

8 Dong, Z., Wang, F., Reese, T.G., Bilgic, B., Setsompop, K., 2020. Echo planar time-resolved imaging  
9 with subspace reconstruction and optimized spatiotemporal encoding. *Magn. Reson. Med.* 84, 2442-2455.

10 Dong, Z., Wang, F., Reese, T.G., Manhard, M.K., Bilgic, B., Wald, L.L., Guo, H., Setsompop, K., 2019. Tilted-CAIPI for highly accelerated distortion-free EPI with point spread function (PSF) encoding. *Magn.*  
11 *Reson. Med.* 81, 377-392.

12 Dong, Z., Wang, F., Wald, L.L., Setsompop, K., 2021b. Accelerated Echo-train shifted EPTI (ACE-  
13 EPTI) for fast distortion-blurring-free high-resolution diffusion imaging with minimal echo time. *Proc. Intl.*  
14 *Soc. Mag. Reson. Med.*, p. 1316.

15 Dumoulin, S.O., Fracasso, A., van der Zwaag, W., Siero, J.C., Petridou, N., 2018. Ultra-high field MRI:  
16 Advancing systems neuroscience towards mesoscopic human brain function. *Neuroimage* 168, 345-357.

17 Duyn, J., 2004. Specificity of high-resolution BOLD and CBF fMRI at 7 T. *Magn. Reson. Med.* 51,  
18 644-645.

19 Fair, M.J., Wang, F., Dong, Z., Reese, T.G., Setsompop, K., 2020. Propeller echo-planar time-resolved  
20 imaging with dynamic encoding (PEPTIDE). *Magn. Reson. Med.* 83, 2124-2137.

21 Feinberg, D., Harel, N., Ramanna, S., Ugurbil, K., Yacoub, E., 2008. Sub-millimeter single-shot 3D  
22 GRASE with inner volume selection for T2-weighted fMRI applications at 7 Tesla. *Proc. Intl. Soc. Mag.*  
23 *Reson. Med.*, 16, 37.

24 Fischl, B., 2012. FreeSurfer. *Neuroimage* 62, 774-781.

25 Fischl, B., Salat, D.H., Busa, E., Albert, M., Dieterich, M., Haselgrove, C., Van Der Kouwe, A.,  
26 Killiany, R., Kennedy, D., Klaveness, S., 2002. Whole brain segmentation: automated labeling of  
27 neuroanatomical structures in the human brain. *Neuron* 33, 341-355.

28 Goense, J.B., Logothetis, N.K., 2006. Laminar specificity in monkey V1 using high-resolution SE-  
29 fMRI. *Magn. Reson. Imaging* 24, 381-392.

30 Goerke, U., Garwood, M., Ugurbil, K., 2011. Functional magnetic resonance imaging using RASER.  
31 *Neuroimage* 54, 350-360.

32 Goerke, U., van de Moortele, P.F., Ugurbil, K., 2007. Enhanced relative BOLD signal changes in T2-  
33 weighted stimulated echoes. *Magn. Reson. Med.* 58, 754-762.

34 Griswold, M.A., Jakob, P.M., Heidemann, R.M., Nittka, M., Jellus, V., Wang, J., Kiefer, B., Haase, A.,  
35 2002. Generalized autocalibrating partially parallel acquisitions (GRAPPA). *Magn. Reson. Med.* 47, 1202-  
36 1210.

37 Guo, R., Zhao, Y., Li, Y., Wang, T., Li, Y., Sutton, B., Liang, Z.P., 2021. Simultaneous QSM and  
38 metabolic imaging of the brain using SPICE: Further improvements in data acquisition and processing.  
39 *Magn Reson Med.* 85, 970-977.

40 Han, S., Liao, C., Manhard, M.K., Park, D.J., Bilgic, B., Fair, M.J., Wang, F., Blazejewska, A.I.,  
41 Grissom, W.A., Polimeni, J.R., 2020. Accelerated spin-echo functional MRI using multisection excitation  
42 by simultaneous spin-echo interleaving (MESSI) with complex-encoded generalized slice dithered  
43 enhanced resolution (cgSlider) simultaneous multislice echo-planar imaging. *Magn Reson Med.* 84, 206-  
44 220.

45 Havlicek, M., Uludağ, K., 2020. A dynamical model of the laminar BOLD response. *NeuroImage* 204,  
46 116209.

47 He, J., Liu, Q., Christodoulou, A.G., Ma, C., Lam, F., Liang, Z.P., 2016. Accelerated High-Dimensional  
48 MR Imaging With Sparse Sampling Using Low-Rank Tensors. *IEEE Trans. Med. Imaging* 35, 2119-2129.

49 Heinze, J., Koopmans, P.J., den Ouden, H.E., Raman, S., Stephan, K.E., 2016. A hemodynamic model  
50 for layered BOLD signals. *Neuroimage* 125, 556-570.

1 Huber, L., Finn, E.S., Chai, Y., Goebel, R., Stirnberg, R., Stöcker, T., Marrett, S., Uludag, K., Kim, S.G., Han, S., 2020. Layer-dependent functional connectivity methods. *Prog. Neurobiol.*, 101835.

2 Huber, L., Handwerker, D.A., Jangraw, D.C., Chen, G., Hall, A., Stüber, C., Gonzalez-Castillo, J., Ivanov, D., Marrett, S., Guidi, M., 2017a. High-resolution CBV-fMRI allows mapping of laminar activity and connectivity of cortical input and output in human M1. *Neuron* 96, 1253-1263. e1257.

3 Huber, L., Ivanov, D., Krieger, S.N., Streicher, M.N., Mildner, T., Poser, B.A., Möller, H.E., Turner, R., 2014. Slab-selective, BOLD-corrected VASO at 7 Tesla provides measures of cerebral blood volume reactivity with high signal-to-noise ratio. *Magn. Reson. Med.* 72, 137-148.

4 Huber, L., Uludağ, K., Möller, H.E., 2019. Non-BOLD contrast for laminar fMRI in humans: CBF, CBV, and CMRO2. *Neuroimage* 197, 742-760.

5 Jenkinson, M., Beckmann, C.F., Behrens, T.E., Woolrich, M.W., Smith, S.M., 2012. *Fsl. Neuroimage* 62, 782-790.

6 Jeong, H.K., Gore, J.C., Anderson, A.W., 2013. High-resolution human diffusion tensor imaging using 2-D navigated multishot SENSE EPI at 7 T. *Magn. Reson. Med.* 69, 793-802.

7 Jin, T., Kim, S.-G., 2006. Spatial dependence of CBV-fMRI: a comparison between VASO and contrast agent based methods. *Conf Proc IEEE Eng Med Biol Soc.*, 25-28.

8 Kemper, V.G., De Martino, F., Vu, A.T., Poser, B.A., Feinberg, D.A., Goebel, R., Yacoub, E., 2015. Sub-millimeter T2 weighted fMRI at 7 T: comparison of 3D-GRASE and 2D SE-EPI. *Front. Neurosci.* 9, 163.

9 Koopmans, P.J., Barth, M., Orzada, S., Norris, D.G., 2011. Multi-echo fMRI of the cortical laminae in humans at 7 T. *Neuroimage* 56, 1276-1285.

10 Koopmans, P.J., Yacoub, E., 2019. Strategies and prospects for cortical depth dependent T2 and T2\* weighted BOLD fMRI studies. *Neuroimage*, 197, 668-676.

11 Kundu, P., Inati, S.J., Evans, J.W., Luh, W.M., Bandettini, P.A., 2012. Differentiating BOLD and non-BOLD signals in fMRI time series using multi-echo EPI. *Neuroimage* 60, 1759-1770.

12 Kundu, P., Voon, V., Balchandani, P., Lombardo, M.V., Poser, B.A., Bandettini, P.A., 2017. Multi-echo fMRI: a review of applications in fMRI denoising and analysis of BOLD signals. *Neuroimage* 154, 59-80.

13 Kwong, K.K., Belliveau, J.W., Chesler, D.A., Goldberg, I.E., Weisskoff, R.M., Poncelet, B.P., Kennedy, D.N., Hoppel, B.E., Cohen, M.S., Turner, R., 1992. Dynamic magnetic resonance imaging of human brain activity during primary sensory stimulation. *Proc. Natl. Acad. Sci.* 89, 5675-5679.

14 Lam, F., Liang, Z.P., 2014. A subspace approach to high-resolution spectroscopic imaging. *Magn. Reson. Med.* 71, 1349-1357.

15 Liang, Z.-P., 2007. Spatiotemporal imaging with partially separable functions. *Proc. IEEE Int. Symp. Biomed. Imaging*, 988-991.

16 Lu, H., Golay, X., Pekar, J.J., Van Zijl, P.C., 2003. Functional magnetic resonance imaging based on changes in vascular space occupancy. *Magn. Reson. Med.* 50, 263-274.

17 Lu, H., Van Zijl, P.C., Hendrikse, J., Golay, X., 2004. Multiple acquisitions with global inversion cycling (MAGIC): a multislice technique for vascular-space-occupancy dependent fMRI. *Magn. Reson. Med.* 51, 9-15.

18 Mani, M., Jacob, M., Kelley, D., Magnotta, V., 2017. Multi-shot sensitivity-encoded diffusion data recovery using structured low-rank matrix completion (MUSSELS). *Magn. Reson. Med.* 78, 494-507.

19 Mareyam, A., Kirsch, J.E., Chang, Y., Madan, G., Wald, L.L., 2020. A 64-Channel 7T array coil for accelerated brain MRI. *Proc. Intl. Soc. Mag. Reson. Med.*, 764.

20 Markuerkiaga, I., Barth, M., Norris, D.G., 2016. A cortical vascular model for examining the specificity of the laminar BOLD signal. *Neuroimage*, 132, 491-498.

21 Meng, Z., Guo, R., Li, Y., Guan, Y., Wang, T., Zhao, Y., Sutton, B., Li, Y., Liang, Z.P., 2021. Accelerating T2 mapping of the brain by integrating deep learning priors with low-rank and sparse modeling. *Magn. Reson. Med.* 85, 1455-1467.

22 Miller, K.L., Hargreaves, B.A., Lee, J., Ress, D., Christopher deCharms, R., Pauly, J.M., 2003. Functional brain imaging using a blood oxygenation sensitive steady state. *Magn. Reson. Med.* 50, 675-683.

1 Norris, D.G., Polimeni, J.R., 2019. Laminar (f) MRI: A short history and future prospects. *NeuroImage* 2 197, 643-649,

3 Norris, D.G., 2012. Spin-echo fMRI: the poor relation? *Neuroimage* 62, 1109-1115.

4 Ogawa, S., Lee, T.-M., Kay, A.R., Tank, D.W., 1990. Brain magnetic resonance imaging with contrast 5 dependent on blood oxygenation. *Proc. Natl. Acad. Sci.* 87, 9868-9872.

6 Ogawa, S., Menon, R., Tank, D., Kim, S., Merkle, H., Ellermann, J., Ugurbil, K., 1993. Functional 7 brain mapping by blood oxygenation level-dependent contrast magnetic resonance imaging. A comparison 8 of signal characteristics with a biophysical model. *Biophys. J.* 64, 803-812.

9 Olman, C.A., Harel, N., Feinberg, D.A., He, S., Zhang, P., Ugurbil, K., Yacoub, E., 2012. Layer- 10 specific fMRI reflects different neuronal computations at different depths in human V1. *PloS one* 7, e32536.

11 Park, S., Torrisi, S., Townsend, J.D., Beckett, A., Feinberg, D.A., 2021. Highly accelerated 12 submillimeter resolution 3D GRASE with controlled blurring in-weighted functional MRI at 7 Tesla: A 13 feasibility study. *Magn. Reson. Med.* 85, 2490-2506.

14 Pfaffenrot, V., Voelker, M.N., Kashyap, S., Koopmans, P.J., 2021. Laminar fMRI using T2-prepared 15 multi-echo FLASH. *Neuroimage*, 118163.

16 Pflugfelder, D., Vahedipour, K., Uludağ, K., Shah, N.J., Stöcker, T., 2011. On the numerically 17 predicted spatial BOLD fMRI specificity for spin echo sequences. *Magn. Reson. Imaging* 29, 1195-1204.

18 Polimeni, J., Zaretskaya, N., Stelzer, J., Bause, J., Ehses, P., Wald, L., Scheffler, K., 2017. 19 Macrovascular contributions to high-resolution balanced SSFP-and GE-EPI-based fMRI at 9.4 T evaluated 20 using surface-based cortical depth analyses in human visual cortex. *Proc. Intl. Soc. Mag. Reson. Med.*, 5255.

21 Poser, B.A., Norris, D.G., 2007. Fast spin echo sequences for BOLD functional MRI. *Magn. Reson. 22 Mater. Phys.* 20, 11.

23 Poser, B.A., Versluis, M.J., Hoogduin, J.M., Norris, D.G., 2006. BOLD contrast sensitivity 24 enhancement and artifact reduction with multiecho EPI: parallel-acquired inhomogeneity-desensitized 25 fMRI. *Magn. Reson. Med.* 55, 1227-1235.

26 Posse, S., Wiese, S., Gembris, D., Mathiak, K., Kessler, C., Grosse-Ruyken, M.L., Elghahwagi, B., 27 Richards, T., Dager, S.R., Kiselev, V.G., 1999. Enhancement of BOLD-contrast sensitivity by single-shot 28 multi-echo functional MR imaging. *Magn. Reson. Med.* 42, 87-97.

29 Pruessmann, K.P., Weiger, M., Scheidegger, M.B., Boesiger, P., 1999a. SENSE: sensitivity encoding 30 for fast MRI. *Magn. Reson. Med.* 42, 952-962.

31 Pruessmann, K.P., Weiger, M., Scheidegger, M.B., Boesiger, P., 1999b. SENSE: sensitivity encoding 32 for fast MRI. *Magn. Reson. Med.* 42, 952-962.

33 Scheffler, K., Seifritz, E., Bilecen, D., Venkatesan, R., Hennig, J., Deimling, M., Haacke, E.M., 2001. 34 Detection of BOLD changes by means of a frequency-sensitive trueFISP technique: preliminary results. 35 *NMR Biomed.* 14, 490-496.

36 Setsompop, K., Fan, Q., Stockmann, J., Bilgic, B., Huang, S., Cauley, S.F., Nummenmaa, A., Wang, 37 F., Rathi, Y., Witzel, T., 2018. High-resolution *in vivo* diffusion imaging of the human brain with 38 generalized slice dithered enhanced resolution: Simultaneous multislice (g S lider-SMS). *Magn. Reson. 39 Med.* 79, 141-151.

40 Setsompop, K., Gagoski, B.A., Polimeni, J.R., Witzel, T., Wedeen, V.J., Wald, L.L., 2012. Blipped- 41 controlled aliasing in parallel imaging for simultaneous multislice echo planar imaging with reduced g- 42 factor penalty. *Magn. Reson. Med.* 67, 1210-1224.

43 Smith, S.M., Jenkinson, M., Woolrich, M.W., Beckmann, C.F., Behrens, T.E., Johansen-Berg, H., 44 Bannister, P.R., De Luca, M., Drobniak, I., Flitney, D.E., 2004. Advances in functional and structural MR 45 image analysis and implementation as FSL. *Neuroimage* 23, S208-S219.

46 Sodickson, D.K., Manning, W.J., 1997. Simultaneous acquisition of spatial harmonics (SMASH): fast 47 imaging with radiofrequency coil arrays. *Magn. Reson. Med.* 38, 591-603.

48 Splitthoff, D., Zaitsev, M., 2009. SENSE shimming (SSH): a fast approach for determining B0 field 49 inhomogeneities using sensitivity coding. *Magn. Reson. Med.* 62, 1319-1325.

50 Tamir, J.I., Uecker, M., Chen, W., Lai, P., Alley, M.T., Vasanawala, S.S., Lustig, M., 2017. T2 shuffling: 51 sharp, multicontrast, volumetric fast spin-echo imaging. *Magn. Reson. Med.* 77, 180-195.

1 van der Kouwe, A.J., Benner, T., Salat, D.H., Fischl, B., 2008. Brain morphometry with multiecho  
2 MPRAGE. *Neuroimage* 40, 559-569.

3 Versluis, M., Sutton, B., De Bruin, P., Börnert, P., Webb, A., Van Osch, M., 2012. Retrospective image  
4 correction in the presence of nonlinear temporal magnetic field changes using multichannel navigator  
5 echoes. *Magn. Reson. Med.* 68, 1836-1845.

6 Waehnert, M., Dinse, J., Weiss, M., Streicher, M.N., Waehnert, P., Geyer, S., Turner, R., Bazin, P.-L.,  
7 2014. Anatomically motivated modeling of cortical laminae. *Neuroimage* 93, 210-220.

8 Waehnert, M.D., Dinse, J., Schäfer, A., Geyer, S., Bazin, P.-L., Turner, R., Tardif, C.L., 2016. A  
9 subject-specific framework for in vivo myeloarchitectonic analysis using high resolution quantitative MRI.  
10 *Neuroimage* 125, 94-107.

11 Wallace, T.E., Afacan, O., Kober, T., Warfield, S.K., 2020. Rapid measurement and correction of  
12 spatiotemporal B0 field changes using FID navigators and a multi-channel reference image. *Magn. Reson.*  
13 *Med.* 83, 575-589.

14 Wang, F., Dong, Z., Reese, T.G., Bilgic, B., Katherine Manhard, M., Chen, J., Polimeni, J.R., Wald,  
15 L.L., Setsompop, K., 2019. Echo planar time-resolved imaging (EPTI). *Magn. Reson. Med.* 81, 3599-3615.

16 Wang, F., Dong, Z., Reese, T.G., Rosen, B., Wald, L.L., Setsompop, K., 2021a. 3D Echo Planar Time-  
17 resolved Imaging (3D-EPTI) for ultrafast multi-parametric quantitative MRI. *bioRxiv*.

18 Wang, F., Dong, Z., Tian, Q., Chen, J., Blazejewska, A.I., Reese, T.G., Polimeni, J.R., Setsompop, K.,  
19 2020. Cortical-depth dependence of pure T2-weighted BOLD fMRI with minimal T2' contamination using  
20 Echo-Planar Time-resolved Imaging (EPTI). *Proc. Intl. Soc. Mag. Reson. Med.* 1229.

21 Wang, F., Dong, Z., Wald, L.L., Polimeni, J.R., Setsompop, K., 2021. Simultaneous pure spin-echo  
22 and gradient-echo BOLD fMRI using Echo Planar Time-resolved Imaging (EPTI) for mapping laminar  
23 fMRI responses. *Proc. Intl. Soc. Mag. Reson. Med.* 631.

24 Yacoub, E., Duong, T.Q., Van De Moortele, P.F., Lindquist, M., Adriany, G., Kim, S.G., Uğurbil, K.,  
25 Hu, X., 2003. Spin-echo fMRI in humans using high spatial resolutions and high magnetic fields. *Magn.*  
26 *Reson. Med.* 49, 655-664.

27